A&A 462, 645–656 (2007)
DOI: 10.1051/0004-6361:20065236

Astronomy & Astrophysics

X-rays from protostellar jets: emission from continuous flows

R. Bonito[1,2], S. Orlando[2], G. Peres[1], F. Favata[3], and R. Rosner[4,5]

[1] Dip. Scienze Fisiche ed Astronomiche, Sez. Astronomia, Università di Palermo, P.zza del Parlamento 1, 90134 Palermo, Italy
e-mail: sbonito@astropa.unipa.it
[2] INAF - Osservatorio Astronomico di Palermo, P.zza del Parlamento 1, 90134 Palermo, Italy
[3] Astrophysics Div. - Research and Science Support Dept. of ESA, ESTEC, Postbus 299, 2200 AG Noordwijk, The Netherlands
[4] Dept. of Astronomy and Astrophysics, Univ. of Chicago, Chicago, IL 60637, USA
[5] Center for Astrophysical Thermonuclear Flashes, University of Chicago, 5640 S. Ellis Avenue, Chicago, IL 60637, USA

Received 20 March 2006 / Accepted 17 October 2006

ABSTRACT

Context. Recently X-ray emission from protostellar jets has been detected with both XMM-*Newton* and *Chandra* satellites, but the physical mechanism which can give rise to this emission is still unclear.
Aims. We performed an extensive exploration of the parameter space for the main parameters influencing the jet/ambient medium interaction. Aims include: 1) to constrain the jet/ambient medium interaction regimes leading to the X-ray emission observed in Herbig-Haro objects in terms of the emission by a shock forming at the interaction front between a continuous supersonic jet and the surrounding medium; 2) to derive detailed predictions to be compared with optical and X-ray observations of protostellar jets; 3) to get insight into the protostellar jet's physical conditions.
Methods. We performed a set of two-dimensional hydrodynamic numerical simulations, in cylindrical coordinates, modeling supersonic jets ramming into a uniform ambient medium. The model takes into account the most relevant physical effects, namely thermal conduction and radiative losses.
Results. Our model explains the observed X-ray emission from protostellar jets in a natural way. In particular, we find that a protostellar jet that is less dense than the ambient medium well reproduces the observations of the nearest Herbig-Haro object, HH 154, and allows us to make detailed predictions of a possible X-ray source proper motion ($v_{\rm sh} \approx 500$ km s^{-1}) detectable with *Chandra*. Furthermore, our results suggest that the simulated protostellar jets which best reproduce the X-rays observations cannot drive molecular outflows.

Key words. shock waves – ISM: Herbig-Haro objects – ISM: jets and outflows – X-rays: ISM

1. Introduction

The early stages of the star birth are characterized by a variety of mass ejection phenomena, including collimated jets. These plasma jets can travel through the interstellar medium at supersonic speed, with shock fronts forming at the interaction front between the jet and the unperturbed ambient medium. In the last 50 years these features have been studied in detail in the radio, infrared, optical and UV bands, and are known as Herbig-Haro (hereafter HH) objects (Herbig 1950; Haro 1952; see also Reipurth & Bally 2001).

Pravdo et al. (2001) predicted that the most energetic HH objects could be sources of strong X-ray emission. Following Zel'dovich & Raizer (1966), one can derive useful relations between the physical parameters of interest in the post-shock region (such as the plasma temperature and the shock velocity), viz.,

$$T_{\rm psh} = \frac{\gamma - 1}{(\gamma + 1)^2} \left(\frac{m v_{\rm sh}^2}{k_{\rm B}} \right), \quad (1)$$

where $T_{\rm psh}$ is the post-shock temperature, γ is the ratio of specific heats, $v_{\rm sh}$ is the shock front speed, m is the mean particle mass and $k_{\rm B}$ is the Boltzmann constant. Assuming a typical velocity, $v_{\rm sh} \approx 500$ km s^{-1} (as measured in HH 154, see Fridlund et al. 2005), the expected post-shock temperature is a few million degrees, thus leading to X-ray emission.

Recently, X-ray emission from HH objects has been detected with both the XMM-*Newton* and *Chandra* satellites: the low mass young stellar objects (YSO) HH 2 in Orion (Pravdo et al. 2001) and HH 154 in Taurus (Favata et al. 2002; Bally et al. 2003), the high mass YSO objects HH 80/81 in Sagittarius (Pravdo et al. 2004) and HH 168 in Cepheus A (Pravdo & Tsuboi 2005), and HH 210 in Orion (Grosso et al. 2006). Indications of X-ray emission from protostellar jets are also discussed by Tsujimoto et al. (2004) and Güdel et al. (2005). A summary of the relevant physical quantities derived for these objects is presented in Table 1.

In addition to the intrinsic interest in the physics, understanding the X-ray emission from protostellar jets is important in the context of the physics of star and planet formation. X-rays (and ionizing radiation in general) affect many aspects of the environment of young stellar objects and, in particular, the physics and chemistry of the accretion disk and its planet-forming environment. The ionization state of the accretion disk around young stellar objects will determine its coupling to the ambient and protostellar magnetic field, and thus, for example, influence its turbulent transport. In turn, this will affect the accretion rate and the formation of structures in the disk and, therefore, the formation of planets. X-rays also can act as catalysts of chemical reactions in the disk's ice and dust grains, thereby significantly affecting its chemistry and mineralogy.

The ability of the forming star to ionize its environment will therefore significantly affect the outcome of the formation process, independent of the origin of the ionizing radiation. While all young stellar objects are strong X-ray sources, they will

Table 1. Relevant physical quantities observed in confirmed X-ray emitting HH objects, where L_X is the reported X-ray luminosity, kT and N_H are respectively the best fit parameters derived from spectral analysis for the temperature (in keV) and for the interstellar absorption column density, v_{sh} is the shock front velocity derived from optical observations, D is the distance of the object observed and L_{bol} is the bolometric luminosity of the jet driving source (Pravdo et al. 2001; Favata et al. 2002; Bally et al. 2003; Pravdo et al. 2004; Pravdo & Tsuboi 2005; Grosso et al. 2006). $L_\odot$ is the solar bolometric luminosity.

Object	L_X [10^{29} erg s^{-1}]	kT [keV]	N_H [10^{22} cm^{-2}]	v_{sh} [km s^{-1}]	D [pc]	$L_{bol}/L_\odot$	L_X/L_{bol}
HH 2	5.2	0.23	≤ 0.09	230	480	81[a]	1.7×10^{-6}
HH 154	3.0	0.34	1.40	500	140	40[b]	9.7×10^{-7}
HH 80/81	450	0.13	0.44	700	1700	2×10^4[c]	1.5×10^{-4}
HH 168	1.1	0.5	0.40	500	730	2.5×10^4[c]	3.6×10^{-7}
HH 210	10	0.07−0.33	0.80	130	450	–	–

[a] Chini et al. (2001). [b] Liseau et al. (2005). [c] Curiel et al. (2006).

irradiate the disk from its center, so that stellar X-rays will illuminate the disk in grazing incidence, concentrating their effects in the central regions of the disk; however, this depends critically on the disk geometry, so that for example flared disks can show more extended regions affected by ionizing radiation. Since protostellar jets are located above the disk, they will illuminate the disk in near normal incidence, maximizing their irradiation effects even in the outer disk regions normally shielded from the stellar X-rays. For example, the X-ray emission from HH 154 is located at some 150 AU from the protostar, ensuring illumination of the disk with favorable geometry out to few hundreds AU.

Several models have been proposed to explain the X-ray emission from protostellar jets, but the actual emission mechanism is still unclear. Bally et al. (2003) speculated on different mechanisms for the X-ray emission from HH 154: X-ray emission from the central star reflected by a dense medium, X-ray emission produced when the stellar wind shocks against the wind from the companion star, or produced in shocks in the jet. Raga et al. (2002) derived a simple analytic model that predicts X-ray emission originating from protostellar jets with the observed characteristics.

Prompted by the recent detection of X-ray emission from HH objects, we developed a detailed hydrodynamic model of the interaction between a supersonic protostellar jet and the ambient medium; our aim is to explain the detailed physics that may lead to the observed X-ray emission. Our model takes into account optically thin radiative losses and thermal conduction effects. We use the FLASH code (Fryxell et al. 2000) with customized numerical modules that treat optically thin radiative losses and thermal conduction (Orlando et al. 2005). The core of FLASH is based on a directionally split Piecewise Parabolic Method (PPM) solver to handle compressible flows with shocks (Colella & Woodward 1984). FLASH uses the PARAMESH library to handle adaptive mesh refinement (MacNeice et al. 2000) and the Message-Passing Interface (MPI) library to achieve parallelization.

In a previous paper (Bonito et al. 2004), we presented a first set of results concerning a jet that is less dense than the ambient medium, with a density contrast $\nu = n_a/n_j = 10$ (where n_a is the ambient density and n_j is the density of the jet); these model results showed X-ray emission in good agreement with the observed X-ray emission from HH 154 (Favata et al. 2002). Bonito et al. (2004) have shown the validity of the physical principle on which our model is based: a supersonic jet traveling through the ambient medium produces a shock at the jet/ambient medium interaction front, leading to X-ray emission in good agreement with observations. In the present paper, we study the effects of varying the control parameters characterizing the jet on the jet dynamics; the control parameters of interest include the ambient-to-jet density ratio, $\nu = n_a/n_j$, and the Mach number, $M = v_j/c_a$ (c_a is the ambient sound speed). By exploring a wide range of the control parameter space, we seek to determine the range of these parameters that can give rise to X-ray emission consistent with observations.

The paper is structured as follow: Sect. 2 describes the model and the numerical setup; in Sect. 3 we discuss the results of our numerical simulations; finally, Sect. 4 is devoted to a summary and our conclusions. In Appendix A we discuss our method for synthesizing the predicted X-ray emission from our numerical simulations.

2. The model

We model the propagation of a continuously driven protostellar jet through an isothermal and homogeneous ambient medium. We assume that the fluid is fully ionized and that it can be regarded as a perfect gas with a ratio of specific heats $\gamma = 5/3$. Finally, we assume that any extant magnetic fields are negligible.

The jet evolution is described by the fluid equations for mass, momentum and energy conservation, taking into account the effects of radiative losses and thermal conduction,

$$\frac{\partial \rho}{\partial t} + \nabla \cdot \rho \boldsymbol{v} = 0 \tag{2}$$

$$\frac{\partial \rho \boldsymbol{v}}{\partial t} + \nabla \cdot \rho \boldsymbol{v}\boldsymbol{v} + \nabla p = 0 \tag{3}$$

$$\frac{\partial \rho E}{\partial t} + \nabla \cdot (\rho E + p)\boldsymbol{v} = -\nabla \cdot q - n_e n_H P(T) \tag{4}$$

where t is the time, ρ the mass density, $\boldsymbol{v}$ the plasma velocity, p the pressure, q the heat flux, n_e and n_H are respectively the electron and hydrogen density, $P(T)$ is the optically thin radiative losses function per unit emission measure ($P(T)$ is described by a functional form that takes into account free-free, bound-free, bound-bound and 2 photons emission; see Raymond & Smith 1977; Mewe et al. 1985; Kaastra & Mewe 2000), T the plasma temperature, and

$$E = \epsilon + \frac{1}{2}|\boldsymbol{v}|^2, \tag{5}$$

where E is the total energy and ϵ is the specific internal energy. We use the equation of state for an ideal gas,

$$p = (\gamma - 1)\rho\epsilon. \tag{6}$$

Following Dalton & Balbus (1993), we use an interpolation expression for the thermal conductive flux of the form

$$q = \left(\frac{1}{q_{\rm spi}} + \frac{1}{q_{\rm sat}}\right)^{-1}, \quad (7)$$

which allows for a smooth transition between the classical and saturated conduction regimes. In the above expression, $q_{\rm spi}$ represents the classical conductive flux (Spitzer 1962)

$$q_{\rm spi} = -\kappa(T)\nabla T, \quad (8)$$

where $\kappa(T) = 9.2\times10^{-7}T^{5/2}$ erg s^{-1} K^{-1} cm^{-1} is the thermal conductivity. The saturated flux, $q_{\rm sat}$, is given by (Cowie & McKee 1977)

$$q_{\rm sat} = -{\rm sign}(\nabla T)5\phi\rho c_{\rm s}^3, \quad (9)$$

where $\phi \sim 0.3$ (Giuliani 1984; Borkowski et al. 1989, and references therein) and $c_{\rm s}$ is the isothermal sound speed.

2.1. Numerical setup

We adopt a 2D cylindrical (r, z) coordinate system, with the jet axis coincident with the z-axis. The computational grid size in dimensional form varies from ≈300 AU to ≈600 AU in the r direction and from ≈6000 AU to $\approx 3 \times 10^4$ AU in the z direction, where the particulars of these dimensions are chosen so that we are able to follow the jet/ambient medium interaction for at least 20–50 years.

In the case of a jet less dense than the ambient medium (hereafter called a "light jet") that best reproduces observations, the integration domain extends over 300 AU in the radial direction and over 6000 AU in the z direction. In the case of the jet with the same initial density as the ambient medium (hereafter referred to as an "equal-density jet") that best reproduces observations, the domain is $(r \times z) \approx (600 \times 6000)$ AU. In this latter case, the radial axis is twice as large as in the light jet case because the cocoon surrounding the equal density jet has a radial extension greater than in the light jet case. The dimension of the computational domain in the case of a jet denser than the ambient medium (hereafter, a "heavy jet") that best reproduces observations is $(r \times z) \approx (700 \times 27\,000)$ AU.

In all of these cases, the initial jet velocity is along the z axis, coincident with the jet axis, and has a radial profile of the form

$$V(r) = \frac{V_0}{\nu\cosh(r/r_j)^w - (\nu - 1)}, \quad (10)$$

where V_0 is the on-axis velocity, ν is the ambient to jet density ratio, $r_{\rm j}$ is the initial jet radius and $w = 4$ is the steepness parameter for the shear layer (as an example, see the continuous line in Fig. 1, for the light jet case discussed in Sect. 3.2, with corresponding parameters given in Table 3), adjusted so as to achieve a smooth transition of the kinetic energy at the interface between the jet and the ambient medium.

The density variation in the radial direction (dashed line in Fig. 1) is given by

$$\rho(r) = \rho_{\rm j}\left(\nu - \frac{\nu - 1}{\cosh(r/r_{\rm j})^w}\right), \quad (11)$$

where $\rho_{\rm j}$ is the jet density (Bodo et al. 1994).

Reflection boundary conditions are imposed along the jet axis, inflow boundary conditions are imposed at $z = 0$ and $r \le r_{\rm j}$, and outflow boundary conditions are assumed elsewhere.

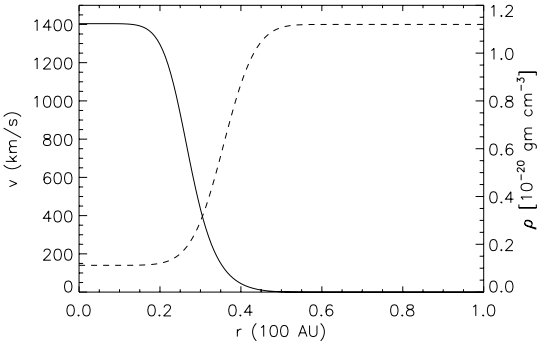

Fig. 1. Initial jet velocity (continuous line) and density (dashed line) as a function of the distance from the axis, r, for the light jet case discussed in Sect. 3.2 with parameters: $M = 300$, $\nu = 10$, $n_{\rm j} = 500$ cm^{-3}, $T_{\rm a} = 10^3$ K, $r_{\rm j} = 30$ AU, $w = 4$ (see Table 3).

The maximum spatial resolution achieved in the best light jet case (in both the r and z directions) is ≈1.3 AU, as determined from the PARAMESH methodology for 4 refinement levels, which corresponds to covering the jet radius with 25 points at the maximum resolution. The spatial resolution achieved in the equal-density case is half that obtained in the light jet case; and the spatial resolution achieved in the best heavy jet model is 8 times lower than in the light jet case.

Our choice of different spatial resolutions for these three cases was dictated by the need to limit the computational cost; this constraint arises because the solver for thermal conduction is explicit in our version of FLASH and, therefore, a time-step limiter depending on density, ρ, temperature, T, and spatial resolution, Δx, is required in order to avoid numerical instability (see, for instance, Orlando et al. 2005). Stability is guaranteed for $\Delta t < 0.5\,\Delta x^2/D$, where D is the diffusion coefficient, related to the conductivity, κ, and to the specific heat at constant volume, c_v, by $D = \kappa(T)/(\rho c_v)$. Thus, calculations involving high temperatures (as, for instance, in the heavy jet case) are especially constrained, and therefore a lower spatial resolution is required in order to avoid a very small time-step, Δt.

2.2. Time scales

Condensations of plasma due to radiative cooling effects can become thermally unstable; however, the presence of thermal conduction can prevent such instabilities. By comparing the radiative, $\tau_{\rm rad}$, and thermal conduction, $\tau_{\rm cond}$, characteristic times

$$\tau_{\rm rad} = \frac{p}{(\gamma - 1)n_{\rm e}n_{\rm H}P(T)} \approx 2.5\times10^3\frac{T^{3/2}}{n} \quad (12)$$

$$\tau_{\rm cond} \approx \frac{p}{\gamma - 1}\frac{7}{2}\frac{l^2}{\kappa(T)T} \approx 1.5\times10^{-9}\frac{nl^2}{T^{5/2}}, \quad (13)$$

where l represents the characteristic length scale of temperature variations, we can infer which of the two competing processes dominates during the jet/ambient medium interaction. From the condition

$$\left(\frac{\tau_{\rm rad}}{\tau_{\rm cond}}\right)^{1/2} = 1 \quad (14)$$

we can derive the cutoff length scale for instability, $l_{\rm F}$ (Field 1965), which indicates the maximum length

$$l_{\rm F} \approx 1.3\times10^6\frac{T^2}{n} \quad (15)$$

Table 2. Range of parameters used in our numerical model (Col. 2) compared with typical outflow parameters (Cols. 3 and 4) shown in Bally & Reipurth (2002), Table 1. ν is the ambient medium to jet density contrast; M is the Mach number; T_a and n_a are the ambient medium temperature and density, respectively; v_j is the initial jet velocity; v_{sh} is the shock velocity of the knots inside the jet; $\dot{M}$ is the mass loss rate; and L_{mech} is the mechanical luminosity.

Parameter	Model	Low mass[a]	High mass[a]	Units
ν	$0.01 \div 300$	–	–	–
M	$1 \div 1000$	–	–	–
T_a	$30 \div 10^6$	–	–	K
n_a	$5 \div 10^5$	–	–	cm^{-3}
v_j	$85 \div 8500$	–	–	km s^{-1}
v_{sh}	$100 \div 2000$	$100 \div 300$	$100 \div 1000$	km s^{-1}
$\dot{M}$	$10^{-10} \div 10^{-8}$	$10^{-9} \div 10^{-5}$	$10^{-6} \div 10^{-2}$	$M_\odot$ yr^{-1}
L_{mech}	$6.7 \times 10^{-5} \div 67$	$0.001 \div 1$	$0.1 \div 1000$	$L_\odot$

[a] Bally & Reipurth (2002).

over which thermal conduction dominates over radiative effects in the classical conduction regime. An analogous estimate in the saturation regime leads to

$$(l_F)_{sat} \approx 3 \times 10^7 \frac{T^2}{n}, \quad (16)$$

which is one order of magnitude longer than the characteristic length in the classical regime. As discussed later in Sect. 3.2, the comparison between the classical Field length (the shortest characteristic length) and the size of the region behind the shock at the head of the jet will allow us to determine if this region is thermally stable or not.

In order to verify our assumption of a fully ionized gas, we computed the ionization time scale of the most relevant elements in the X-ray spectrum of a shocked plasma at $T = 3.4 \times 10^6$ K, assuming a post-shock density of about 10^4 cm^{-3} (the light jet case). As an example, we can show that the ionization time scale for C and O is 1 to 2 orders of magnitudes smaller than the radiative and thermal conduction time scales, so that the plasma indeed can be considered to be in ionization equilibrium.

2.3. Parameters

Our model solutions depend upon a number of physical parameters, such as, for instance, the jet and ambient temperature and density, the jet velocity and its radius. In order to reduce the number of free parameters in our exploration of the parameter space, we have fixed the jet radius to $r_j \approx 30$ AU, following Favata et al. (2002) (who found this characteristic linear scale from the X-ray thermal fit), and Fridlund et al. (2005) (who showed HST images of the internal knots of HH 154 with dimension $r \approx 30$ AU at the base of the jet[1]). However, detailed simulations with different r_j values are not necessary since we can predict the effects of varying the jet radius from the model results we obtained so far. In fact we expect the X-ray emitting region to grow in size as r_j grows. Since the X-ray luminosity is defined as $L_X = n^2 V P(T)$, it depends on the cube of the radius. This means that, as L_X is constrained from observations, a jet with a greater radius needs a lower density in order to reproduce observations. We impose an initial jet length $z_j = 300$ AU in order to avoid the ejected plasma that travels back inside the boundary during the jet evolution. This choice of a non-zero initial jet length allows us to obtain an unperturbed boundary surface at $z = 0$. In all our simulations, we model a jet with initial density and temperature $n_j = 500$ cm^{-3} and $T_j = 10^4$ K, respectively, following the values derived from observations (Fridlund & Liseau 1998; Favata et al. 2002). The density and temperature of the ambient medium, n_a and T_a respectively, are derived from the choice of the ambient medium-to-jet density contrast, ν and from the hypothesis of initial pressure balance between the ambient medium and the jet. We are left, therefore, with two non-dimensional control parameters: the jet Mach number, M, and the ambient medium-to-jet density contrast, ν. For a more extended exploration of the parameter space, see Sect. 3.5, which explores the variation of the initial jet density, n_j. In our simulations we account for the wide jet/ambient medium parameters range shown in Table 2.

In Sect. 3, we discuss the results derived from the exploration of the parameter space defined by M and ν.

3. Results

3.1. Exploration of the parameter space

We performed a broad exploration of the control parameter space defined by the two free parameters, the jet Mach number, $M = v_j/c_a$, and the ambient medium-to-jet density ratio, $\nu = n_a/n_j$ (see Sect. 2.3). The aim is to determine the range of parameters leading to X-ray emission from protostellar jets that is in agreement with the observations.

We first analyzed adiabatic hydrodynamic models, i.e., models without thermal conduction and radiative losses. Then, for the most promising cases (i.e., for those adiabatic cases that most closely reproduce the values of jet velocity, temperature and luminosity of the X-ray source derived from the observations), we performed more realistic simulations in which we have taken into account thermal conduction and radiative loss effects. By comparing these latter models with those without thermal conduction and radiative cooling, we are able to explore how the presence of these physical processes affects the jet/ambient medium system evolution. We found that, in general, models with thermal conduction and radiation reach lower temperatures (up to 5 times lower than those achieved in the adiabatic cases). We also found that thermal conduction smoothes the density and temperature spatial structures that are well visible in the pure hydrodynamic cases.

In the following subsections, we discuss the models (shown in Fig. 2) in which both radiative losses and thermal conduction are taken into account. In Fig. 2 green and red dots refer to those cases with X-ray luminosity $L_X > 10^{28}$ erg s^{-1}, shock front velocity $v_{sh} > 100$ km s^{-1} and fitting temperature $T < 10^7$ K, consistent with observations. We have chosen L_X one order of magnitude lower than the minimum value observed (see Table 1) in order to take into account fainter sources that have not as yet been detected; the red dot refers to the representative case of HH 154 discussed in Bonito et al. (2004). Squares show cases with velocities in the range of values observed, but with $L_X < 10^{28}$ erg s^{-1}; diamonds mark the cases with velocities and X-ray luminosity not consistent with observations; and triangles mark cases with temperatures higher than 10^7 K. The lower panel of Fig. 2 shows the initial velocity assumed in our simulations vs. the density contrast.

[1] In Fridlund et al. (2005), page 993, the authors discuss the working surface. The radius quoted is that of the elongated Mach disk (probably representative of the jet), and is ≈30 AU. The separation between the Mach disk and the working surface is 0.6″ or 4 times this ≈100 AU (M. Fridlund, private communication).

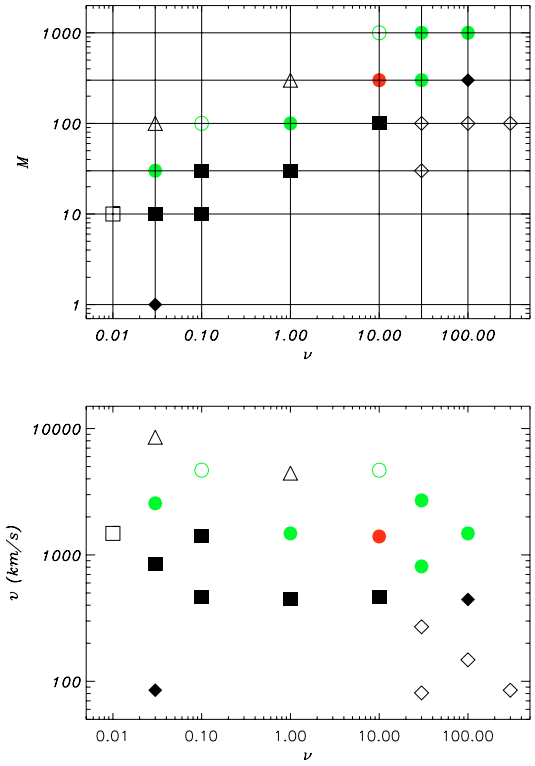

Fig. 2. Exploration of the parameter space: jet Mach number, M (*upper panel*) and initial jet velocity (*lower panel*) as a function of the ambient-to-jet density contrast, ν. Green and red dots refer to models consistent with observations for X-ray luminosity, shock velocity and fitting temperature values (see text); diamonds refer to models which cannot reproduce observations; squares refer to models in good agreement with observations for shock velocity but not for X-ray luminosity values; triangles refer to models with too high ($T \geq 10^7$ K, one order of magnitude higher than observed) temperature. Empty symbols refer to pure hydrodynamic simulations; filled symbols refer to models in which thermal conduction and radiative losses effects are taken into account.

Table 3. Summary of the initial physical parameters characterizing the "best-fit" models in the case of light, equal-density and heavy jets: ambient-to-jet density contrast, ν, jet Mach number, M, initial jet velocity, v_j, ambient density and the temperature, n_a, and T_a, respectively. In all the models, the initial jet density and temperature are $n_j = 500$ cm^{-3} and $T_j = 10^4$ K, respectively.

Model	ν	M	v_j [km s^{-1}]	n_a [cm^{-3}]	T_a [10^4 K]
light	10	300	1400	5000	0.1
equal-density	1	100	1500	500	1
heavy	0.03	30	2500	17	30

From our exploration of the parameter space, we are able to show that the models in agreement with observations lie within a well constrained region in our parameter space. In the following sections, we discuss in detail the "best-fit" models, i.e., those models that reproduce X-ray luminosity and shock front speed values as close as possible to those observed, for the three cases of light, equal-density and heavy jets (see Table 3).

3.2. Hydrodynamic evolution

In Fig. 3, we show the mass density and temperature distributions 20 years after the beginning of the jet/ambient medium interaction for the three best-fit models in Table 3. The light jet case best reproduces the physical parameters derived from observations by Fridlund & Liseau (1998) and Favata et al. (2002) for the HH 154 protostellar jet; its properties have been discussed in Bonito et al. (2004).

In all cases, there is clear evidence at the head of the jet of a shock front due to the plasma propagating supersonically along the jet axis. Just behind the shock front there is a localized hot and dense "blob" that can be seen clearly, for instance, in the enlargement of the shock front shown in Fig. 4 for the light jet case.

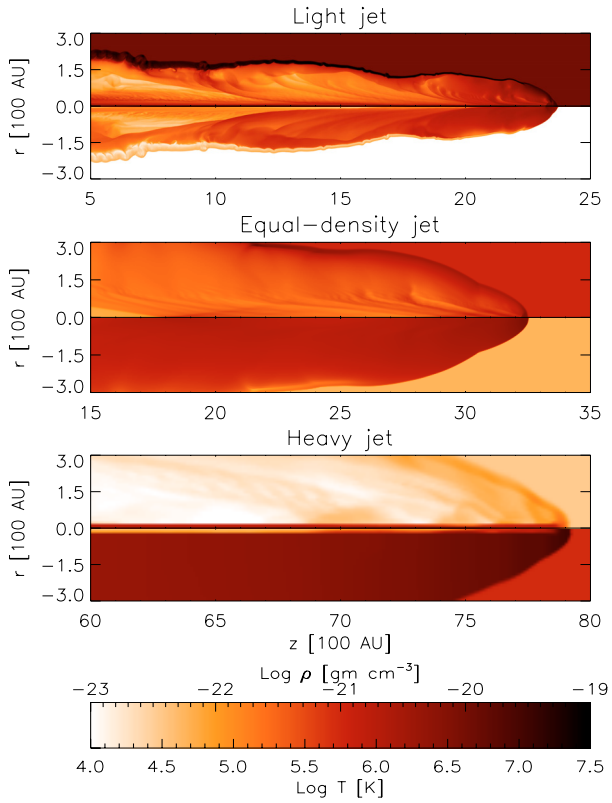

Fig. 3. Two-dimensional mass density (*upper half-panels*) and temperature (*lower half-panels*) cuts in the $r - z$ plane after 20 years since the beginning of the jet/ambient medium interaction for the best cases of light (*upper panels*), equal-density (*middle panels*) and heavy jets (*lower panels*).

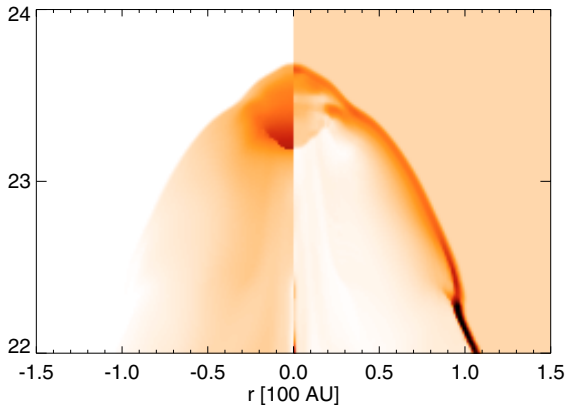

Fig. 4. An enlargement of the post shock region in the light jet case for temperature (*left*) and density (*right*) in linear scale, obtained about 20 years after the beginning of the jet/ambient medium interaction. Note the hot and dense region just behind the shock front.

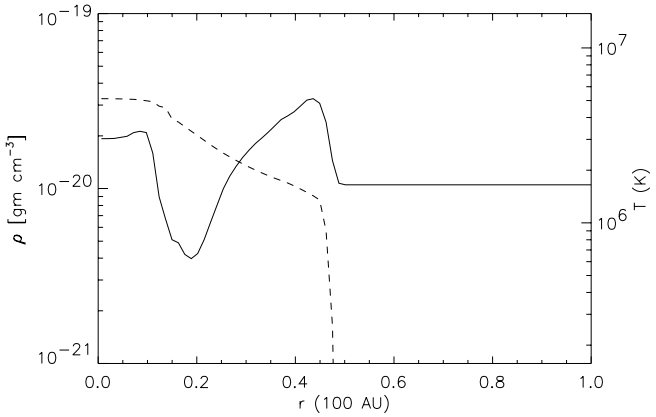

Fig. 5. Density (continuous line) and temperature (dashed line) profiles along the radial direction at $z \approx 5000$ AU, corresponding to the blob position at $t = 40$ yr ($M = 300$, $v = 10$).

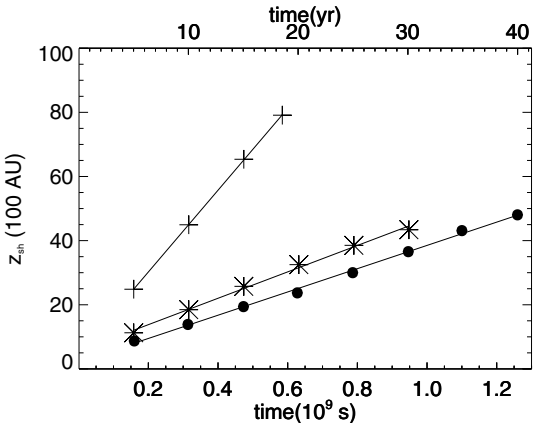

Fig. 6. Shock front position vs. time. Dots mark the light jet case, stars the equal-density jet, and crosses the heavy jet case. The lines refer to the best fit, from which we derive the average shock speed: $v_{sh} \approx 500$ km s^{-1}, $\approx$600 km s^{-1}, $\approx$1900 km s^{-1} for the light, equal-density and heavy jet case, respectively.

The light jet is enveloped by a cocoon whose temperature T ($\approx 7 \times 10^5$ K) is spatially almost uniform due to thermal conduction; nevertheless, the cocoon temperature is not constant in time but decreases as the evolution proceeds, leading to the formation of a cool and dense external envelope. Figure 5 shows traces of the density (continuous line) and temperature (dashed line) along the radius at $z \approx 5000$ AU, corresponding to the blob position 40 years since the beginning of the jet/ambient medium interaction: the hot (few million degrees) and dense blob is evident for $r < 10$ AU. The density decreases moving away from the jet axis along the radial direction, then increases again at the position corresponding to the external part of the cocoon. In contrast, the temperature monotonically decreases as one moves away from the jet axis along the radial direction. The blob therefore is expected to be an X-ray source; in Sect. 3.4.2, we will show that this X-ray source has a luminosity and spectral characteristics consistent with those observed.

The central double panel in Fig. 3 shows 2D sections in the (r, z) plane of the mass density and temperature distributions for the best-fit equal-density model (see Table 3). The interaction between the protostellar jet and the ambient medium leads to a dense and hot cocoon ($n \approx 1400$ cm^{-3}; $T \approx 2 \times 10^6$ K) surrounding the jet. Once again, the cocoon's temperature is spatially almost uniform (because of thermal conduction), and this temperature decreases with time. Thus, this cocoon gradually cools and becomes denser with time, just as in the light-jet case. Again, the post-shock region shows evidence for a hot and dense blob from which the X-ray emission originates (see Sect. 3.4.1 for more details).

In the heavy-jet case (lower double panel in Fig. 3), the jet is surrounded by a cocoon that is well smoothed by the effects of thermal conduction and whose radial extension is larger than that in the other two cases. The cocoon has temperature of a few million degrees, and its density is lower than that of the jet.

For the three best-fit models just discussed, we analyzed the thermal stability of the hot and dense blob localized behind the shock by comparing the size of the blob with the Field length, Eq. (15). In the light jet case, the values obtained for the average blob temperature, $T \approx 3.4 \times 10^6$ K, and density, $n \approx 6500$ cm^{-3}, lead to $l_F \sim 100$ AU. Since the blob size (which is almost equal to twice the initial jet radius $r_j \approx 30$ AU; see Fig. 4) is smaller than l_F, it appears that the blob is thermally stable. In the equal-density jet case, the density and temperature of the blob at the head of the jet are $n \approx 1700$ cm^{-3} and $T \approx 4.3 \times 10^6$, respectively, leading to $l_F \approx 10^3$ AU. Also in this case, therefore, we can conclude that the blob is thermally stable, given that its size ($\sim$100 AU) is roughly 10 times smaller than the Field length. Finally, in the heavy-jet case, the temperature and density of the blob are $T \sim 10^7$ K and $n \sim 10^2$ cm^{-3}, leading to $l_F \approx 10^4$ AU. Since the blob behind the shock front now extends over $\sim$100 AU, it is thermally stable in this case as well. To summarize: in all of the cases considered in which the predicted X-ray properties agree with observations, we find that the emitting "blob" is thermally stable.

The position of the shock front as a function of time for the three best-fit models in Table 3 is shown in Fig. 6. For the light jet case, we derived an average shock velocity $v_{sh} \approx 500$ km s^{-1}, about 3 times lower than the initial jet velocity. This shock velocity is in good agreement with observed speeds in HH objects, and in particular with that derived from HH 154 data. Taking into account the jet inclination $\approx$45 degrees (Fridlund & Liseau 1998), $v_{sh} \approx 500$ km s^{-1} corresponds to a proper motion of $\approx$350 km s^{-1}, which (at the distance of HH 154) can be measured with well time-spaced *Chandra* observations.

In the equal-density jet scenario, we deduced an average shock velocity $v_{sh} \approx 600$ km s^{-1}, slightly greater than the value observed in HH 154 (Fridlund & Liseau 1998; Favata et al. 2002), but consistent with values observed in other HH objects (see Table 1). For the heavy jet case, the average value of the shock speed is $v_{sh} \approx 1900$ km s^{-1} which is too high with respect to the HH shock front velocities observed (cf. Table 1).

3.3. Emission measure distribution vs. temperature

We derived the distribution of emission measure vs. temperature, $EM(T)$, in the temperature range [10^3–10^8] K at different stages of the evolution of the jet/ambient medium system (see Appendix A for more details). Figure 7 shows the $EM(T)$ for the three best-fit models in Table 3, 20 years after the beginning of the jet/ambient medium interaction.

In all of these cases, we find that the shape of the $EM(T)$ is characterized by two bumps, and does not change significantly during the system evolution. The relative weight of the bumps is different in the three cases. In the light jet case (upper panel in Fig. 7), the bumps are quite broad, the first centered at temperature $T \sim 10^4$ K with $EM \sim 10^{55}$ cm^{-3}, and the second one

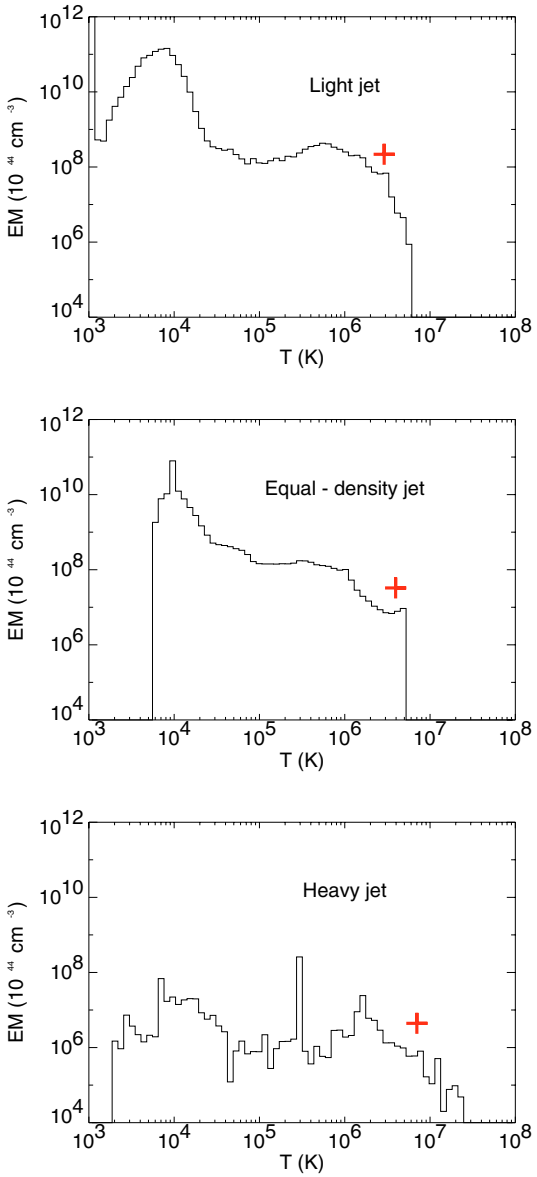

Fig. 7. Emission measure, EM, as a function of the temperature, T for the three models discussed in the text, at a time 20 years after the beginning of the jet/ambient medium interaction. The cross superimposed on each panel marks the best-fit temperature and emission measure values derived from our simulated absorbed spectra.

centered at $T \sim 10^6$ K with $EM \sim 10^{52}$ cm^{-3}, about three orders of magnitude lower than the first bump; the EM decreases rapidly above few millions degrees.

In the equal-density jet case (middle panel in Fig. 7), the first bump is centered at $T \sim 10^4$ K with $EM \geq 10^{54}$ cm^{-3}, whereas the second bump is centered at $T \sim 10^6$ K with $EM \sim 10^{52}$ cm^{-3}, just as in the light jet case. Finally, in the heavy jet case (lower panel in Fig. 7), the $EM(T)$ distribution appears flat, with two weak peaks centered at $T \sim 10^4$ K and at a few million degrees. Note that in the heavy jet case, the EM at temperatures up to a few million degrees is two orders of magnitude lower than in the light jet case.

On the basis of these $EM(T)$ distributions, we expect a bright ($L_X > 10^{28}$ erg s^{-1}) X-ray source, whose soft component (due to the cocoon) could be suppressed by the strong interstellar medium absorption (Favata et al. 2002). We also expect that the X-ray emission decreases as the ambient medium-to-jet density ratio, ν, decreases, leading to brighter X-ray emission in the light jet case.

3.4. X-ray emission

From the $EM(T)$ distributions and the MEKAL spectral code, we have synthesized the focal plane spectra as predicted to be detected with the instruments on board XMM-*Newton* and *Chandra* (see Appendix A for details); in deriving these predictions, we have taken into account interstellar absorption. In order to compare our numerical models with experimental data concerning HH 154 (the closest and best studied jet emitting in the X-ray band), we assumed a distance of 150 pc (as HH 154 is located in the L1551 cloud in the Taurus star-forming region) and an interstellar absorption column density $N_H = 1.4 \times 10^{22}$ cm^{-2} (Favata et al. 2002). Our model results can be generalized to account for the other HH objects observations by considering different values for the distance and the interstellar absorption.

3.4.1. Spatial distribution of the X-ray emission

Assuming that the jet propagates perpendicularly to the line of sight, we computed predicted X-ray images of the jet/ambient medium system from our numerical simulations, to be compared with images obtained with the high spatial resolution *Chandra*/ACIS-I instrument (see Appendix A). For all the models in Table 3, we are able to show that most of the X-ray emission produced during the jet/ambient medium interaction originates from a very compact region localized at the head of the jet, just behind the shock front.

Figure 8 shows an enlargement of the head of the jet (where most of the X-ray emission originates) of our predicted X-ray images, to be compared with *Chandra*/ACIS-I images; our predicted images are assumed to correspond to the jet 20 years after the beginning of the jet/ambient medium interaction. Note that the spatial resolution of the synthesized X-ray images in Fig. 8 is 6 times better than that of the *Chandra*/ACIS-I. In all three cases analyzed, a comparison between the X-ray emitting region and the temperature and density maps in Fig. 3 shows that the X-ray source is coincident with the hot and dense blob discussed in Sect. 3.2.

We find that even with *Chandra*'s high spatial resolution, the predicted X-ray emitting region cannot be spatially resolved, and so we expect that it will be detected as a point-like source. Furthermore, we expect that significant X-ray emission will be seen only from the hot and dense blob behind the shock front, as the softer cocoon emission is likely to be extinguished by the strong interstellar absorption.

As discussed in Sect. 3.2, the X-ray emitting region for the three cases examined is thermally stable, and therefore the X-ray emission should be continuously detectable during the 20–50 years analyzed. We also found that there are no significant variations of the X-ray source morphology during the evolution: the source size varies by ±25%, always below the spatial resolution achievable with *Chandra*. However, for some of the cases shown in Fig. 2, our analysis predicts transient behaviour of the X-ray source, which extinguishes a few years after the beginning of the interaction between the protostellar jet and the ambient medium, because of radiative cooling that dominates thermal conduction effects.

From Fig. 6, the X-ray source coincident with the hot and dense blob discussed in Sect. 3.2 has a proper motion of

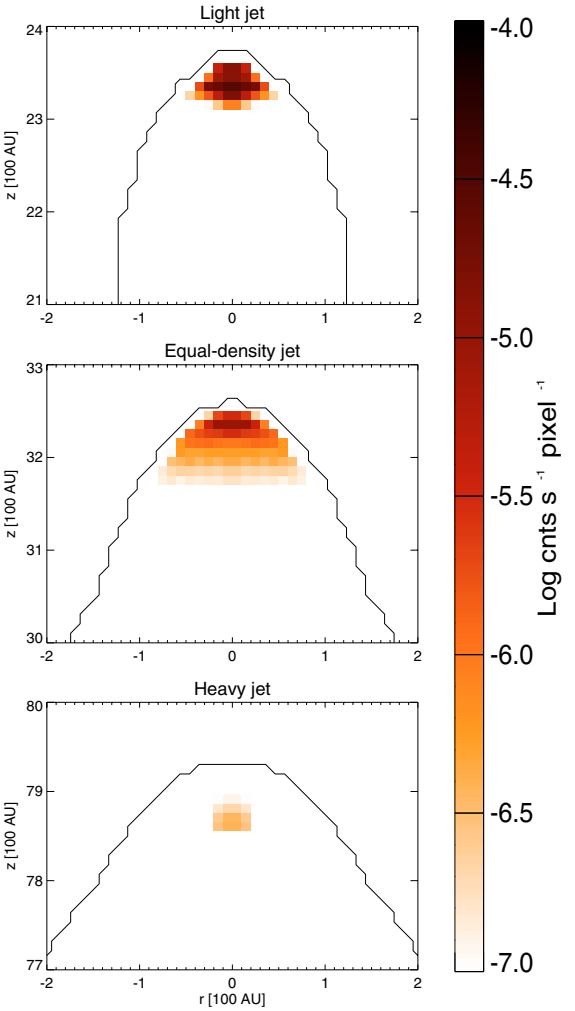

Fig. 8. Synthesized X-ray emission, in logarithmic scale, as predicted to be observed with ACIS-I, for the three cases examined, 20 years since the beginning of the jet/ambient medium interaction. At a distance $D \approx$ 150 pc, 100 AU corresponds to about 0.7 arcsec.

~0.7 arcsec/yr, ~0.8 arcsec/yr, and ~2.7 arcsec/yr in the light, equal-density and heavy jet cases, respectively, under the assumption that the jet axis is perpendicular to the line of sight. In addition, we find that the intensity of the X-ray source decreases about one order of magnitude as the ambient medium-to-jet density contrast, ν, decreases. Note that the heavy jet case has the higher shock front speed and the lower X-ray emission.

3.4.2. Spectral analysis

We derived the synthesized focal plane spectra predicted to be observed with XMM-*Newton*/EPIC-pn, an instrument characterized by a large effective area, with the aim of comparing our model results with published data and, in particular, with those data concerning HH 154 (Favata et al. 2002).

We considered two different levels of count statistics in the [0.3−10] keV band: in the low statistics case, we have fixed the exposure time so as to obtain about 100 total photons for each spectrum, whereas in the high statistics case, we imposed about 10^4 counts for each spectrum. Although the latter case is unrealistic (given the low photon counts so far collected from these sources), it can help us to pinpoint some of fundamental features of the predicted spectra. The spectral bins are grouped together to have at least 10 photons in the low count statistics case and 20 photons in the other case.

For the light and equal-density jet models, the synthesized spectra are well described by emission from an optically thin plasma at a single temperature, even in the high count statistics case. This result is due to the strong interstellar absorption which suppresses the soft emission originating from the cooler plasma component in the cocoon. The best fit parameters derived from our simulations are shown in Table 4.

The heavy jet model which best fits HH observations shows more structured spectra than those obtained in the light jet and equal-density jet cases: in the high statistics case, the spectra are well described by a two temperature component plasma emission model, with the best fit parameters reported in Table 4.

The spectral analysis of course reflects the structure of the $EM(T)$ distribution: the spectra are mostly sensitive to the high temperature portion of the $EM(T)$ (see Fig. 7), as the softer component is suppressed by the interstellar medium absorption. On the other hand, in the heavy jet model, the $EM(T)$ distribution is characterized by a broader bump at high temperatures than is found in the other two cases (see Fig. 7), implying that the underlying high temperature distribution is more complex than a single temperature model.

Figure 9 shows the evolution of the X-ray luminosity, L_X, in the [0.3−10] keV band, derived from the isothermal components fitted to the spectra in the high statistics case. The light jet case (dots in Fig. 9) shows L_X values in good agreement with those observed in HH 154 ($L_X = 3 \times 10^{29}$ erg s^{-1}, see Favata et al. 2002). In the equal-density jet case, L_X ranges between 7.4×10^{28} and 2.7×10^{29} erg s^{-1}, in general below the luminosity observed in HH 154, although its values are consistent with those detected in other HH objects (see Table 1). On the other hand, in the heavy jet case, the L_X values (crosses in Fig. 9) are at least one order of magnitude lower than those observed so far in HH objects (Table 1), and in HH 154 in particular.

3.5. Varying the jet density parameter

As an extension of the exploration of the parameter space, we have varied the value of the initial jet density, n_j, which has so far been fixed to the value derived by Fridlund & Liseau (1998) for HH 154 (namely $n_j = 500$ cm^{-3}). In particular, we performed numerical simulations of a jet with initial density $n_j = 5000$ cm^{-3} (ten times denser than the ambient medium, $\nu = 0.1$) and Mach number $M = 20$, corresponding to an initial jet velocity $v_j \approx 950$ km s^{-1}. We found that this model is thermally unstable since the size of the X-ray emitting region at the head of the jet is larger than the corresponding characteristic Field length. As a consequence, the X-ray luminosity drops over 2 orders of magnitude (starting initially from $\approx 3 \times 10^{29}$ erg/s) in about 10 years.

Higher values of the X-ray emission could be obtained in cases with: 1) higher initial jet density, n_j; 2) higher ambient medium-to-jet density contrast, ν; 3) higher initial jet velocity, v_j.

To account for the first option (higher n_j), we performed the same numerical simulation discussed above, but with an initial jet density 10 times greater, namely $n_j = 5 \times 10^4$ cm^{-3}. In this case, we derived a shock front velocity $\approx$800 km s^{-1} and an X-ray luminosity ranging between 3 and 30×10^{29} erg/s and emission consistent with HH observation in general, but too high to reproduce the observations of HH 154. Such initial jet density values turn out to be much higher than those derived from observations of HH objects. Podio et al. (2006) studied several

Table 4. Best-fit parameters for the EPIC-pn simulated X-ray spectra obtained in the low and high statistics cases, respectively, for the three best-fit models of Table 3, about 20 yr since the beginning of the jet/ambient medium interaction.

Model	Counts	$N_H \pm \Delta N_H$ (10^{22} cm^{-2})	$T_1 \pm \Delta T_1$ (10^6 K)	$EM_1 \pm \Delta EM_1$ (10^{52} cm^{-3})	$T_2 \pm \Delta T_2$ (10^6 K)	$EM_2 \pm \Delta EM_2$ (10^{52} cm^{-3})	χ^2	Prob.[a]
Light	102	1.4 ± 0.3	2.9 ± 1.2	2.5 ± 10.9	–	–	0.44	0.88
	10317	1.39 ± 0.02	2.9 ± 0.1	2.2 ± 0.6	–	–	0.73	1.00
Equal-density	71	1.3 ± 0.4	3.1 ± 3.8	0.4 ± 3.5	–	–	0.49	0.75
	10134	1.38 ± 0.02	3.9 ± 0.2	0.33 ± 0.09	–	–	0.72	1.00
Heavy	92	1.4 ± 0.2	6.8 ± 1.7	0.9 ± 3.4	–	–	0.39	0.93
	9811	1.40 ± 0.04	3.0 ± 0.1	0.2 ± 0.2	11.8 ± 0.4	0.016 ± 0.002	0.73	0.99

[a] Null hypothesis probability.

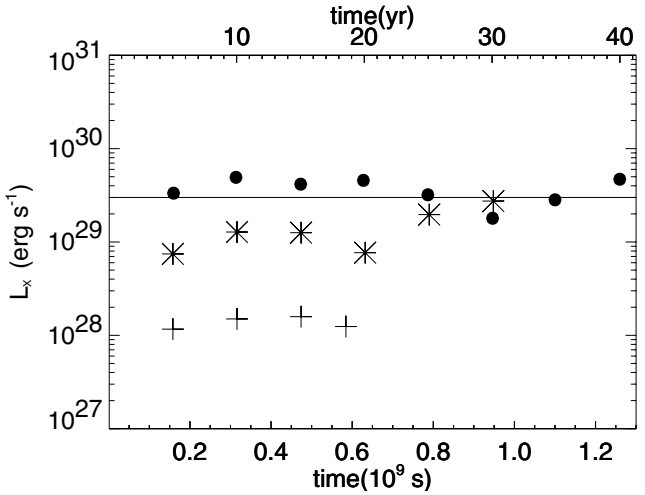

Fig. 9. X-ray luminosity evolution as a function of time. Dots mark the light jet case, stars the equal-density jet, and crosses the heavy jet case. The line superimposed on this figure marks $L_X = 3 \times 10^{29}$ erg s^{-1}, the value observed in HH 154 (Favata et al. 2002).

HH objects, and derived principal physical properties such as their density; in particular, they found that the density ranges between 400 and 1000 cm^{-3} (see also Fridlund & Liseau 1998, for density values in HH 154).

Finally, as far as the second and third options discussed above are concerned, we expect (based on our exploration of the parameter space, Fig. 2) that for a fixed initial jet velocity, the X-ray luminosity will increase with increasing ν and vice versa. Again, we conclude that the jet must be less dense than the ambient medium and/or the jet's initial velocity must be higher than 950 km s^{-1}. Once again, our analysis leads to the conclusion that X-ray emission originating from protostellar jets (in particular, from HH 154) is better reproduced by light jets with an initial jet density $n_j = 500$ cm^{-3}.

4. Discussion and conclusions

We presented a hydrodynamic model that describes the interaction between a supersonic protostellar jet and a homogeneous ambient medium. The aim is to derive the physical parameters of a protostellar jet that can give rise to X-ray emission consistent with recent observations of HH objects.

In a previous paper (Bonito et al. 2004), we have shown the feasibility of the physical principle on which our model is based: a supersonic protostellar jet leads to X-ray emission from the shock, formed at the interaction front with the surrounding gas, consistent with the observations in the particular case of HH 154, the nearest and best studied X-ray emitting protostellar jet. Here we have performed an extensive exploration of a broad region of the parameter space that describes the interaction of the jet/ambient medium system, the parameter space defined by the jet Mach number, M, and the ambient medium-to-jet density contrast, ν (Fig. 2). These results therefore allow us to study and diagnose the physical properties of protostellar jets over a broader range of physical conditions than that defined by HH 154; and thereby our extensive exploration of the parameter space improves and extends the previous work by allowing us to constrain the main protostellar jets parameters in order to obtain X-ray emission, best fit temperature and shock front speed consistent with experimental data. One of the main results of our analyses is that only a narrow range of parameters can reproduce observations.

The ranges of the control parameters which significantly influence the jet/ambient medium evolution are shown in Table 2. From a comparison with observed quantities (also shown in Table 2, according to Bally & Reipurth 2002) we conclude that the parameters used in our models are consistent with observed values. Note however that the values of initial jet velocity are higher than the observed values. This apparent discrepancy is due to the fact that observers measure the velocity of the knots which have already been slowed down by the interaction with the ambient medium. Hence, we need a higher initial jet velocity to account for these currently observed speed values at the working surface. In the best light jet case, we derive a kinetic power $L_{mech} \approx 0.3\ L_\odot$, more than 2 orders of magnitude lower than the observed bolometric luminosity of HH 154, $L_{bol} \approx 40\ L_\odot$ (see Table 1). Thus, the jet velocity values used in our simulations lead to reasonable small kinetic power. Furthermore, comparing the X-ray luminosity derived in the best light jet model here discussed, we deduce that only a small fraction of the kinetic power is converted into X-ray emission: $L_X/L_{mech} \approx (8 \times 10^{-5}\ L_\odot)/(0.3\ L_\odot) = 3 \times 10^{-4}$.

After these preliminaries, we can now proceed to summarize our main findings:

– *Light jet* ($\nu > 1$).
The light jet cases which reproduce the X-ray emission and optical proper motion observed are those with initial Mach number $M \geq 300$ and ambient medium-to-jet density contrast $10 \leq \nu < 100$. For Mach numbers lower than $M = 300$, the X-ray luminosity derived from our simulations is lower than the minimum value observed in protostellar jets ($(L_X)_{obs} > 10^{28}$ erg s^{-1}) and, in some cases, shows transient behaviour due to thermal instabilities. The values $M = 300$ and $\nu = 10$ provide the best case which reproduces the HH 154 observations in terms of best fit temperature, emission measure and X-ray luminosity. We also predict a substantial proper motion.

– *Equal-density jet* ($\nu = 1$).
The three equal-density jet cases analyzed allow us to constrain the initial Mach number of an equal-density protostellar jet to reproduce observations: $30 < M < 300$. From the equal-density model with $M = 100$ we derive shock front velocities and X-ray luminosities consistent with HH objects observations in general (see Table 1).
– *Heavy jet* ($\nu < 1$).
In order to reproduce some characteristics of the observations in the heavy jet scenario, we require an initial jet Mach number $M \approx 30$ and an initial jet density much higher than the ambient density, $\nu \leq 0.03$, i.e., a jet 30 times denser than the ambient medium or more. Lower initial Mach number in some cases leads to thermal instability, which in turn suppress X-ray emission about 5 years after the beginning of the interaction between the protostellar jet and the ambient medium. For a jet 30 times denser than the ambient medium ($\nu = 0.03$) and with initial Mach number $M = 30$, we predict emission from a million degree plasma. Although its $v_{\rm sh}$ is too high and its $L_{\rm X}$ is too low with respect to those observed in HH objects in general (see Table 1) and in HH 154 in particular (Favata et al. 2002), we cannot reject the possibility of new more sensitive observations which may show fainter emission not yet detected in X-ray emitting HH objects.

Here we discussed light, heavy and equal-density jet models that are in best agreement with experimental results from HH objects in general: a light jet with $M = 300$ and $\nu = 10$; an equal-density jet with $M = 100$ and $\nu = 1$; and a heavy jet with $M = 30$ and $\nu = 0.03$. For each case, we analyzed the evolution of the mass density and temperature spatial distributions derived from our model, the shock front proper motion and its spectral properties, the X-ray emission and its stability. In each best-fit model, the interaction between the supersonic protostellar jet and the unperturbed ambient medium leads to the formation of a hot and dense cocoon surrounding the jet and smoothed by thermal conduction. Just behind the shock front, there is a hot and dense blob from which the harder, bright X-ray emission originates: the strong interstellar absorption suppresses the softer component due to the cocoon. In all cases examined, the X-ray emitting region is thermally stable, i.e., thermal conduction prevent the collapse of the source due to radiative cooling; furthermore, this X-ray emitting region should show a detectable proper motion.

To compare our findings with HH 154 observations, we have rejected equal-density and heavy jet cases that show a too large shock front velocity ($v_{\rm sh} \approx 600$ km s^{-1} and ≈ 1900 km s^{-1}, respectively) and too small X-ray luminosity ($L_{\rm X} \approx 10^{29}$ erg s^{-1} and $\approx 10^{28}$ erg s^{-1}), all judged with respect to the $v_{\rm sh}$ and $L_{\rm X}$ values observed in HH 154 ($v_{\rm sh} \approx 500$ km s^{-1} and $L_{\rm X} = 3 \times 10^{29}$ erg s^{-1}).

In the best light jet case, we derive a particle density $n \approx 6500$ cm^{-3} and a velocity $v_{\rm sh} \approx 500$ km s^{-1} for the X-ray emitting region, leading to a momentum $mv = 2 \times 10^{-6}\ M_\odot$ km s^{-1}. This value is consistent with the upper limit $7 \times 10^{-4}\ M_\odot$ km s^{-1} obtained for HH 154 (Fridlund & Liseau 1998). This leads to the conclusion that the protostellar jet cannot drive the molecular outflow, whose momentum has been estimated to be between 0.15 and 1.5 $M_\odot$ km s^{-1} (Fridlund & Liseau 1998). This conclusion is based on the relations for the jet mass loss rate and the mechanical luminosity, given by

$$\dot{M} = 1.8 \times 10^{-9} \frac{M_\odot}{\rm yr} \times \left(\frac{r_{\rm j}}{5 \times 10^{14}\ {\rm cm}}\right)^2 \left(\frac{n_{\rm j}}{500\ {\rm cm^{-3}}}\right)\left(\frac{v_{\rm j}}{1400\ {\rm km\,s^{-1}}}\right), \quad (17)$$

$$L_{\rm mech} = 0.3\ L_\odot \times \left(\frac{r_{\rm j}}{5 \times 10^{14}\ {\rm cm}}\right)^2 \left(\frac{n_{\rm j}}{500\ {\rm cm^{-3}}}\right)\left(\frac{v_{\rm j}}{1400\ {\rm km\,s^{-1}}}\right)^3; \quad (18)$$

these expressions allow us to conclude that the jet mass loss rate and mechanical luminosity are, respectively, 3 and 2 orders of magnitude lower than expected in CO outflows (Cabrit & Bertout 1992). This result supports the conclusion discussed by Fridlund & Liseau (1998) that the jet origin is probably different from that of the CO outflow.

We estimated the values of the momentum, mass loss rate and mechanical luminosity for each model that better reproduce the X-ray observation of HH objects shown in Table 3. We derived: $\dot{M} \sim 10^{-9}\ M_\odot$/yr; $L_{\rm mech} = (0.3{-}1.7)\ L_\odot$; $mv \lesssim 10^{-6}\ M_\odot$ km s^{-1}. These values are several orders of magnitude lower than those observed in CO outflows (in HH 2, HH 154 and HH 80/81, Moro-Martín et al. 1999; Fridlund & Liseau 1998; Yamashita et al. 1989). From the comparison between our results and the observations of CO outflows, we conclude that the simulated protostellar jets which best reproduce X-ray observations cannot drive molecular outflow.

On the basis of our analysis, we conclude that the light jet scenario, with a jet 10 times less dense than the ambient medium ($\nu = 10$) and with an initial jet Mach number $M = 300$, with $v_{\rm sh} \approx 500$ km s^{-1} and $L_{\rm X} \approx 3 \times 10^{29}$ erg s^{-1}, is the best case to reproduce the HH 154 observations. This conclusion is also supported by the optical observations of HH 154 (Fridlund et al. 2005) from which the light jet scenario can be deduced, according to the Hartigan (1989) model.

More generally, in Fig. 10 we show the values of $L_{\rm X}$ vs. T derived from the spectra synthesized from our model as a function of different values of M and ν. Crosses mark cases with $M = 1000$, stars with $M = 300$, diamonds with $M = 100$, triangles with $M = 30$ and squares with $M = 10$. Bigger symbol sizes correspond to higher values of the ambient medium-to-jet density contrast, ν, in the range 0.01 to 300, as in Fig. 2. The shaded zone marks the range of parameters consistent with observation (Table 1). We have chosen $L_{\rm X}$ one order of magnitude lower than the minimum observed so far to account for fainter sources.

For a fixed value of M, $L_{\rm X}$ and T decrease with increasing ν and, for a fixed value of ν, $L_{\rm X}$ and T increase with increasing M. From the figure it is possible to derive M and ν (the velocity and density) of the protostellar jet to be compared with observations (in terms of $L_{\rm X}$ and best fit T). Predictions about possible fainter – not yet discovered – sources can also be made.

Furthermore the results derived from the variation of the initial jet density parameter, $n_{\rm j}$, discussed in Sect. 3.5, lead to the conclusion that, even with different initial density values, a protostellar jet must be less dense than the ambient medium, and must have a high initial velocity (1000 km s^{-1} or more) in order to reproduce HH objects observations.

Our model predicts in all cases a significant proper motion of the X-ray source, with values which, in the case of HH 154 would be measurable with *Chandra*, providing a clear test of the model scenario.

As discussed by Favata et al. (2006), a 100 ks observation was performed in 2005, showing, when compared with the 2001 observation, a more complex scenario, i.e., both a moving and a stationary source were detected in HH 154, giving the source (in 2005) a "knotty" appearance. Thus, while a traveling shock (likely based on the basic physics explored in the present work) is apparently present in HH 154, the source structure is more complex.

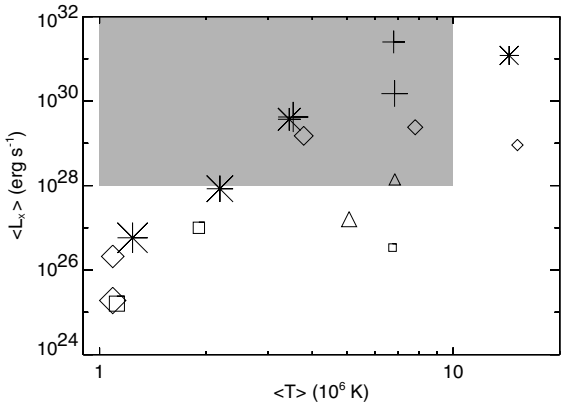

Fig. 10. Mean value of the X-ray luminosity as a function of the mean value of the best fit temperature, derived from our model synthesized spectra. Crosses correspond to Mach number $M = 1000$, stars to $M = 300$, diamonds to $M = 100$, triangles to $M = 30$ and squares to $M = 10$. The increasing size of each symbol corresponds to increasing value of the ambient medium-to-jet density contrast, $\nu = 0.01$-300. The shaded region refers to the (L_X, T) values consistent with observations of HH objects in general.

The comparison between our model of a continuous supersonic jet through an unperturbed surrounding medium and the new *Chandra* data, discussed in Favata et al. (2006), shows that the model reproduces most of the physical properties observed in the X-ray emission of the protostellar jet (temperature, emission measure, etc.). At the same time, it fails to explain the complex evolving observed morphology, showing, most likely, that the jet is not continuous.

A possible scenario that will be tested in the future is based on similar physics as discussed in the present work, but in the presence of pulsating jets (instead of the constant jet inflow here examined); alternatively, it is worthwhile to consider the interactions between the jet and an inhomogeneous ambient medium, which can lead to the knotty structure observed inside the jet itself. We also plan to explore other physical mechanisms, different from the moving shock at the tip of a supersonic jet, stimulated by the above mentioned *Chandra* observations of HH 154, such as steady shocks formed at the mouth of a de Laval nozzle. New observations of the evolution of HH 154 will however be necessary in order to understand the phenomenon and to further constrain the model scenario.

The constant jet inflow model discussed here is a useful and necessary building block towards more complex (e.g., with a discontinuous time profile) models. The X-ray emission from a pulsed jet, for example, will still take place at the shock front, and will thus be based on the same physical effects and principles as observed in a constant inflow jet. Our (simpler) constant inflow jet model is a very useful tool to infer the right parameter values to use in future, more complex models needed to also reproduce the observed morphology: using our constant inflow jet model results, shown in Fig. 2 and in Fig. 10, it is possible to derive the initial jet velocity and ambient medium-to-jet density ratio needed for the new bullets to produce a X-ray luminosity and best fit temperature consistent with observations.

A limitation of our hydrodynamic model is the hypothesis of pressure balance between the jet and the ambient medium, in order to obtain the observed jet collimation. Most models of jet collimation suggest the presence of an organized ambient magnetic field which is known to be effective in collimating the plasma. As a follow-up of our analysis, we are developing an MHD model of protostellar jets that will allow us to relax the assumption of an initial pressure equilibrium. The comparison of the MHD model results with the X-ray observations will provide a fundamental tool to investigate the role of the magnetic field on the protostellar jet dynamics and emission.

Acknowledgements. We would like to thank M. Fridlund for stimulating discussions and the referee for his helpful comments. The software used in this work was in part developed by the DOE-supported ASC/Alliances Center for Astrophysical Thermonuclear Flashes at the University of Chicago, using modules for thermal conduction and optically thin radiation constructed at the Osservatorio Astronomico di Palermo. The calculations were performed on the cluster at the SCAN (Sistema di Calcolo per l'Astrofisica Numerica) facility of the INAF – Osservatorio Astronomico di Palermo and at CINECA (Bologna, Italy). This work was partially supported by grants from CORI 2005, by Ministero Istruzione Università e Ricerca and by INAF.

Appendix A: Synthesizing the X-ray spectra

From our 2D numerical simulations, we synthesized the absorbed focal plane spectra to be compared with observations by using the following procedure.

As a first step, from the integration of the hydrodynamic Eqs. (2), (3) and (4), we derive the temperature and density 2D distributions in the computational domain. We then reconstruct the 3D spatial distribution of these physical quantities by rotating the 2D slabs around the symmetry axis. This allows us to derive the emission measure, defined as $EM = \int n_e n_H dV$ (where n_e and n_H are the electron and hydrogen densities, respectively, and V is the volume of emitting plasma).

From the 3D spatial distributions of T and EM, we derive the distribution of emission measure $EM(T)$ for the computational domain as a whole or for part of it: we consider the temperature range $[10^3$–$10^8]$ K, divided into 74 bins equispaced in $\log T$; the total EM in each temperature bin is obtained by summing the emission measure of all the fluid elements corresponding to the same temperature bin.

From the $EM(T)$, using the MEKAL spectral code (Mewe et al. 1985) for optically thin plasmas, we derive the number of photons in the ith energy bin as follows:

$$I_i = \frac{1}{4\pi D^2} \sum_k \int_{E_i}^{E_{i+1}} \frac{P(T_k, E) EM(T_k)}{E} dE, \quad (A.1)$$

where D is the distance of the object from us, E_i is the energy in the ith bin, $P(T_k, E)$ describes the radiative losses as a function of energy and of the temperature in the kth bin.

To compare our model results with observations, we synthesize the focal plane spectrum, C_i, as predicted to be observed with the *Chandra*/ACIS-I or XMM-*Newton*/EPIC-pn X-ray imaging spectrometers, taking explicit account of the spectral instrumental response:

$$C_i = \frac{t_{exp}}{4\pi D^2} \sum_k \int_{E_i}^{E_{i+1}} A(E) M(i, E) \times \frac{P(T_k, E) EM(T_k)}{E} dE, \quad (A.2)$$

where t_{exp} is the exposure time, $A(E)$ is the energy-dependent effective area and $M(i, E)$ is the instrumental response.

Finally, we take into account the interstellar medium absorption column density, N_H (Morrison & McCammon 1983), and analyze the absorbed focal plane spectrum with XSPEC V11.2 in order to compare our findings with published observational results.

References

Bally, J., & Reipurth, B. 2002, in Rev. Mex. Astron. Astrofis. Conf. Ser., ed. W. J. Henney, W. Steffen, L. Binette, & A. Raga, 1
Bally, J., Feigelson, E., & Reipurth, B. 2003, ApJ, 584, 843
Bodo, G., Massaglia, S., Ferrari, A., & Trussoni, E. 1994, A&A, 283, 655
Bonito, R., Orlando, S., Peres, G., Favata, F., & Rosner, R. 2004, A&A, 424, L1
Borkowski, K. J., Shull, J. M., & McKee, C. F. 1989, ApJ, 336, 979
Cabrit, S., & Bertout, C. 1992, A&A, 261, 274
Chini, R., Ward-Thompson, D., Kirk, J. M., et al. 2001, A&A, 369, 155
Colella, P., & Woodward, P. R. 1984, J. Comput. Phys., 54, 174
Cowie, L. L., & McKee, C. F. 1977, ApJ, 211, 135
Curiel, S., Ho, P. T. P., Patel, N. A., et al. 2006, ApJ, 638, 878
Dalton, W. W., & Balbus, S. A. 1993, ApJ, 404, 625
Favata, F., Fridlund, C. V. M., Micela, G., Sciortino, S., & Kaas, A. A. 2002, A&A, 386, 204
Favata, F., Bonito, R., Micela, G., et al. 2006, A&A, 450, L17
Field, G. B. 1965, ApJ, 142, 531
Fridlund, C. V. M., & Liseau, R. 1998, ApJ, 499, L75
Fridlund, C. V. M., Liseau, R., Djupvik, A. A., et al. 2005, A&A, 436, 983
Fryxell, B., Olson, K., Ricker, P., et al. 2000, ApJS, 131, 273
Güdel, M., Skinner, S. L., Briggs, K. R., et al. 2005, ApJ, 626, L53
Giuliani, J. L. 1984, ApJ, 277, 605
Grosso, N., Feigelson, E. D., Getman, K. V., et al. 2006, A&A, 448, L29
Haro, G. 1952, ApJ, 115, 572
Hartigan, P. 1989, ApJ, 339, 987
Herbig, G. H. 1950, ApJ, 111, 11
Kaastra, J. S., & Mewe, R. 2000, in Atomic Data Needs for X-ray Astronomy, 161
Liseau, R., Fridlund, C. V. M., & Larsson, B. 2005, ApJ, 619, 959
MacNeice, P., Olson, K. M., Mobarry, C., de Fainchtein, R., & Packer, C. 2000, Comput. Phys. Comm., 126, 330
Mewe, R., Gronenschild, E. H. B. M., & van den Oord, G. H. J. 1985, A&AS, 62, 197
Moro-Martín, A., Cernicharo, J., Noriega-Crespo, A., & Martín-Pintado, J. 1999, ApJ, 520, L111
Morrison, R., & McCammon, D. 1983, ApJ, 270, 119
Orlando, S., Peres, G., Reale, F., et al. 2005, A&A, 444, 505
Podio, L., Bacciotti, F., Nisini, B., et al. 2006, A&A, 456, 189
Pravdo, S. H., & Tsuboi, Y. 2005, ApJ, 626, 272
Pravdo, S. H., Feigelson, E. D., Garmire, G., et al. 2001, Nature, 413, 708
Pravdo, S. H., Tsuboi, Y., & Maeda, Y. 2004, ApJ, 605, 259
Raga, A. C., Noriega-Crespo, A., & Velázquez, P. F. 2002, ApJ, 576, L149
Raymond, J. C., & Smith, B. W. 1977, ApJS, 35, 419
Reipurth, B., & Bally, J. 2001, ARA&A, 39, 403
Spitzer, L. 1962, Physics of Fully Ionized Gases (New York: Interscience)
Tsujimoto, M., Koyama, K., Kobayashi, N., et al. 2004, PASJ, 56, 341
Yamashita, T., Suzuki, H., Kaifu, N., et al. 1989, ApJ, 347, 894
Zel'dovich, Y. B., & Raizer, Y. P. 1966, Physics of Shock Waves and High-Temperature Hydrodynamic Phenomena (New York: Academic Press)